EXTRACELLULAR CURRENTS AND POTENTIALS OF THE ACTIVE MYELINATED NERVE FIBER

N. GANAPATHY AND J. W. CLARK, JR.
Department of Electrical and Computer Engineering, Rice University, Houston, Texas 77251-1892

ABSTRACT This paper is concerned with the accurate and rapid calculation of extracellular potentials and currents from an active myelinated nerve fiber in a volume conductor, under conditions of normal and abnormal conduction. The neuroelectric source for the problem is characterized mathematically by using a modified version of the distributed parameter model of L. Goldman and J. S. Albus (1968, *Biophys. J.*, 8:596–607) for the myelinated nerve fiber. Solution of the partial differential equation associated with the model provides a waveform for the spatial distribution of the transmembrane potential $V(z)$. This model-generated waveform is then used as input to a second model that is based on the principles of electromagnetic field theory, and allows one to calculate easily the spatial distribution for the potential everywhere in the surrounding volume conductor for the nerve fiber. In addition, the field theoretic model may be used to calculate the total longitudinal current in the extracellular medium ($I_L^o(z)$) and the transmembrane current per unit length ($i_m(z)$); both of these quantities are defined in connection with the well-known core conductor model and associated cable equations in electrophysiology. These potential and current quantities may also be calculated as functions of time and as such, are useful in interpreting measured $I_L^o(t)$ and $i_m(t)$ data waveforms. An analysis of the accuracy of conventionally used measurement techniques to determine $I_L^o(t)$ and $i_m(t)$ is performed, particularly with regard to the effect of electrode separation distance and size of the volume conductor on these measurements. Also, a simulation of paranodal demyelination at a single node of Ranvier is made and its effects on potential and current waveforms as well as on the conduction process are determined. In particular, our field theoretic model is used to predict the temporal waveshape of the field potentials from the active, non-uniformly conducting nerve fiber in a finite volume conductor.

INTRODUCTION

The study of currents and potentials in and around active myelinated nerve fibers is a subject of great interest in electrophysiology. The effects of demyelination on the nerve fiber's ability to conduct an action potential and the nature of conduction after the myelin sheath grows back some days after the nerve fiber is demyelinated, are but a few of the many aspects of myelinated nerve fiber conduction that are studied using extracellular current and potential measurements from an excised myelinated nerve fiber situated in a finite volume conductor (Paintal, 1965, 1966; Rasminsky and Sears, 1972; Bostock and Sears, 1978; Bostock et al., 1983). Magnetic measurements of action currents have also been obtained by Wikswo et al. (1980) from a vertebrate nerve trunk, and by Barach et al. (1985) and Roth and Wikswo (1985) from an invertebrate nerve cord containing unmyelinated axons. Previous work (Clark and Plonsey, 1968) produced a model based on the principles of electromagnetic field theory that can be easily modified to rapidly and accurately calculate the potential and current density distribution, everywhere in the finite cylindrical volume conductor that bathes the active nerve fiber. The input data required for the calculation consist of the transmembrane potential distribution $\Phi_m(z)$ and the specific conductivities of the intra- and extracellular media. Simulated transmembrane potential data are used in this theoretical study into the nature of the potentials and currents flowing around the single myelinated fiber under conditions of normal and abnormal conduction.

MODELING ASPECTS

The expressions for the intracellular and extracellular potential distributions $\Phi^i(\rho, z)$ and $\Phi^o(\rho, z)$ from an active nerve fiber of radius a positioned at the center of a finite volume conductor of radius b (Fig. 1) may be obtained by solving Laplace's equation under conditions of quasistationarity. The general form of these solutions is given as

$$\Phi^i(\rho, z) = \frac{1}{2\pi}\int_{-\infty}^{\infty} A(k)I_0(|k|\rho)e^{-jkz}\,dk \qquad \rho < a \qquad (1)$$

$$\Phi^o(\rho, z) = \frac{1}{2\pi}\int_{-\infty}^{\infty} [B(k)I_0(|k|\rho) + C(k)K_0(|k|\rho)]e^{-jkz}\,dk \qquad a < \rho < b, \qquad (2)$$

where I_n and K_n are modified Bessel functions of the first and second kind order n. Since axial symmetry ($\partial/\partial\phi = 0$) is assumed, only order $n = 0$ is of interest here. The

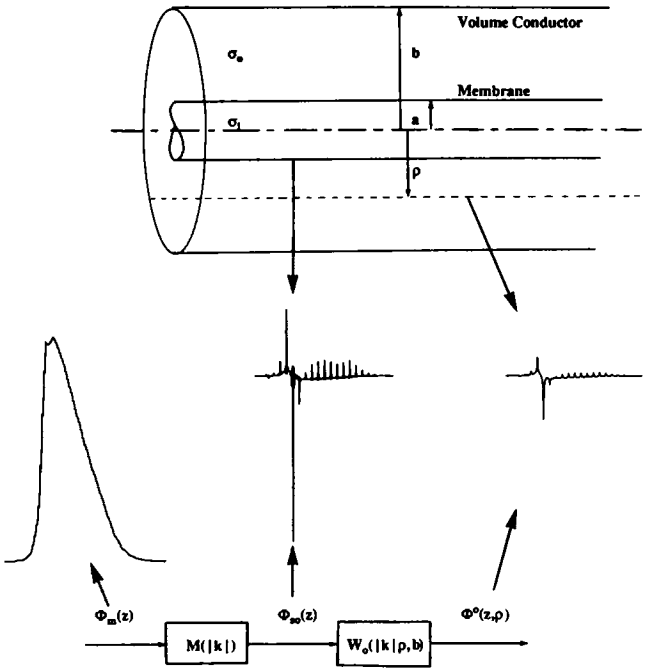

FIGURE 1 A stylized diagram of the equivalent filtering problem for the extracellular potential where $\Phi_m(z)$, $\Phi_{so}(z)$, and $\Phi^o(z, \rho)$ are the spatial transmembrane, outer membrane surface, and field potential distributions, respectively. The membrane filter is $M(|k|)$ and $W_o(|k|\rho, b)$ is the medium filter. Immediately above the block diagram are representative waveforms of the spatial transmembrane, outer membrane surface, and field potential distributions. Fiber geometry is shown at the top of the figure. The external medium is considered uniform, homogeneous, and isotropic with a specific conductivity σ_o (S/cm); the internal medium is assumed to be uniform, homogeneous, and isotropic and is characterized by a specific conductivity σ_i. The fiber radius is denoted by a and the volume conductor radius is b.

coefficients $A(k)$, $B(k)$, and $C(k)$ can be solved for by applying the following boundary conditions at $\rho = a$ and $\rho = b$.

At $\rho = a$,

$$-\sigma_i \frac{\partial \Phi^i}{\partial \rho}\bigg|_a = -\sigma_o \frac{\partial \Phi^o}{\partial \rho}\bigg|_a \tag{3}$$

$$\Phi^i(a^-, z) = \Phi_{si}(z) \tag{4}$$

$$\Phi^o(a^+, z) = \Phi_{so}(z), \tag{5}$$

where $\Phi_{si}(z)$ and $\Phi_{so}(z)$ are potential distributions in z along the inner and outer surfaces of the membrane, respectively.

At $\rho = b$, the sheath-like boundary may be either conductive or nonconductive. In our consideration we will consider it to be nonconductive, that is

$$\frac{\partial \Phi^o}{\partial \rho}\bigg|_b = 0 \tag{6}$$

Upon applying the boundary conditions and after performing some algebraic manipulations, the expressions for intracellular and extracellular potential distributions may be written as

$$\Phi^i(\rho, z) = \frac{1}{2\pi}\int_{-\infty}^{\infty} \frac{I_0(|k|\rho)}{I_0(|k|a)\Delta(|k|)} F_m(k) e^{-jkz}\, dk \qquad \rho \le a^- \tag{7}$$

and

$$\Phi^o(\rho, z) = \frac{1}{2\pi}\int_{-\infty}^{\infty}\left[I_0(|k|\rho) + \frac{I_1(|k|b)}{K_1(|k|b)} K_0(|k|\rho)\right] \frac{F_m(k)}{\Delta(|k|)\eta(|k|)} e^{-jkz}\, dk \qquad a^+ \le \rho \le b, \tag{8}$$

where the quantities $\eta(|k|)$ and $\Delta(|k|)$ are defined as

$$\eta(|k|) \equiv \frac{\sigma_o}{\sigma_i} I_0(|k|a)\left[1 - \frac{I_1(|k|b)K_1(|k|a)}{I_1(|k|a)K_1(|k|b)}\right] \tag{9}$$

and

$$\Delta(|k|) \equiv 1 - \frac{\sigma_i}{\sigma_o}\frac{1 + \dfrac{I_1(|k|b)K_0(|k|a)}{I_0(|k|a)K_1(|k|b)}}{1 - \dfrac{I_1(|k|b)K_1(|k|a)}{I_1(|k|a)K_1(|k|b)}}. \tag{10}$$

Here σ_o and σ_i are the specific conductivities (S/cm) of the extra- and intracellular media. The terms I_n and K_n are modified Bessel functions of the first and second kind, respectively, and of order n; the term $F_m(k)$ is the Fourier transform of the spatial transmembrane potential distribution $\Phi_m(z)$ (Note: $\Phi_m(z) \equiv \Phi_{si}(z) - \Phi_{so}(z)$).

Using the definition of the extracellular field potential (8) the expression for transmembrane current per unit length $i_m(z)$ may be expressed as

$$i_m(z) = -2\pi a\sigma_o \frac{\partial \Phi^o}{\partial \rho}\bigg|_a = -\sigma_o a \int_{-\infty}^{\infty}\left[I_1(|k|a) - \frac{I_1(|k|b)}{K_1(|k|b)} K_1(|k|a)\right] \frac{|k|F_m(k)}{\Delta(|k|)\eta(|k|)} e^{-jkz}\, dk. \tag{11}$$

The derived expressions for potential given by Eqs. 7 and 8 allow one to determine the potential everywhere in the intra- and extracellular media. Based on these expressions, it is possible to compute the current density field anywhere in these media and hence the total longitudinal currents $I_L^i(z)$ and $I_L^o(z)$, associated with the cable equations. In general, the current density field $\bar{J}$ in each of these media consists of a radial and axial component, that is

$$\bar{J}^o(\rho, z) = J_\rho^o(\rho, z)\bar{a}_\rho + J_z^o(\rho, z)\bar{a}_z \tag{12}$$

$$\bar{J}^i(\rho, z) = J_\rho^i(\rho, z)\bar{a}_\rho + J_z^i(\rho, z)\bar{a}_z \tag{13}$$

where

$$J_\rho^o(\rho, z) = -\sigma_o \frac{\partial \Phi^o(\rho, z)}{\partial \rho} \tag{14}$$

$$J_z^o(\rho, z) = -\sigma_o \frac{\partial \Phi^o(\rho, z)}{\partial z} \tag{15}$$

$$J_\rho^i(\rho, z) \equiv -\sigma_i \frac{\partial \Phi^i(\rho, z)}{\partial \rho} \tag{16}$$

$$J_z^i(\rho, z) \equiv -\sigma_i \frac{\partial \Phi^i(\rho, z)}{\partial z} \tag{17}$$

and $\bar{a}_\rho$ and $\bar{a}_z$ are the unit directional vectors.

The expressions for total longitudinal current in each of these media is

$$I_L^o(z) = \int_a^b 2\pi\rho J_z^o(\rho, z)d\rho = -2\pi\sigma_o \int_a^b \rho \frac{\partial \Phi^o(\rho, z)}{\partial z} d\rho \tag{18}$$

$$I_L^i(z) = \int_0^a 2\pi\rho J_z^i(\rho, z)d\rho = -2\pi\sigma_i \int_0^a \rho \frac{\partial \Phi^i(\rho, z)}{\partial z} d\rho. \tag{19}$$

We proceed by using the expressions for potential 7 and 8, differentiating them with respect to z, interchanging the order of integration and evaluating the integral in ρ by using the Bessel function identities (Abramowitz and Stegun, 1965) given as

$$\int_{x_1}^{x_2} x^n K_{n-1}(x)dx = -[x^n K_n(x)]_{x_1}^{x_2} \tag{20}$$

$$\int_{x_1}^{x_2} x^n I_{n-1}(x)dx = [x^n I_n(x)]_{x_1}^{x_2}. \tag{21}$$

The results for the total longitudinal currents are

$$I_L^o(z) = -a\sigma_o \int_{-\infty}^{\infty} \frac{jkF_m(k)}{|k|\Delta(|k|)\eta(|k|)} \left[I_1(|k|a) - \frac{I_1(|k|b)}{K_1(|k|b)} K_1(|k|a)\right] e^{-jkz}dk \tag{22}$$

and

$$I_L^i(z) = a\sigma_i \int_{-\infty}^{\infty} \frac{jkF_m(k)}{I_0(|k|a)\Delta(|k|)} \left[\frac{I_1(|k|a)}{|k|}\right] e^{-jkz}dk. \tag{23}$$

The problem of calculating currents and potential in terms of the integral Eqs. 8, 11, and 22, is simplified by definition of the following set of filter functions:

$$M(|k|) \equiv \frac{1}{\Delta(|k|)} - 1 \tag{24}$$

$$W_o(|k|\,\rho, b) \equiv \left[I_0(|k|\,\rho) + \frac{I_1(|k|\,b)}{K_1(|k|b)} K_0(|k|\,\rho)\right] \frac{1}{\eta(|k|)\{1 - \Delta(|k|)\}} \tag{25}$$

$$C_{mo}(|k|, a, b) \equiv \left\{I_1(|k|\,a) - \frac{I_1(|k|\,b)}{K_1(|k|\,b)} K_1(|k|\,a)\right\} \frac{|k|}{\Delta(|k|)\eta(|k|)} \tag{26}$$

$$C_{Lo}(k, a, b) \equiv \left\{I_1(|k|\,a) - \frac{I_1(|k|\,b)}{K_1(|k|\,b)} K_1(|k|\,a)\right\} \frac{k}{|k|\,\Delta(|k|)\eta(|k|)}, \tag{27}$$

where $M(|k|)$ is the cell membrane filter function used to calculate the potential distribution at the outer surface of the membrane, $W_o(|k|\,\rho, b)$ is the medium filter function used to calculate the extracellular potential and is defined in association with Eq. 8, $C_{mo}(|k|, a, b)$ is a transmembrane current filter function (Eq. 11), and $C_{Lo}(k, a, b)$ is the external longitudinal current filter function (Eq. 22). Thus,

$$\Phi^o(\rho, z) = \frac{1}{2\pi} \int_{-\infty}^{\infty} W_o(|k|\,\rho, b) M(|k|) F_m(k) e^{-jkz}dk \tag{28}$$

$$i_m(z) = -\sigma_o a \int_{-\infty}^{\infty} C_{mo}(|k|, a, b) F_m(k) e^{-jkz}dk \tag{29}$$

and

$$I_L^o(z) = -\sigma_o a \int_{-\infty}^{\infty} C_{Lo}(k, a, b)[jF_m(k)] e^{-jkz}dk. \tag{30}$$

Discrete Fourier Methods of Solution

In the preceding paragraphs, integral expressions have been developed for a number of variables including extracellular potential $\Phi^o(\rho, z)$, transmembrane current per unit length $i_m(z)$, and the total intracellular and extracellular longitudinal current, $I_L^i(z)$ and $I_L^o(z)$, respectively. Computation of these quantities is greatly facilitated by reformulation of these integral expressions in terms of the methodology of the Discrete Fourier Transform (DFT) technique (Greco et al., 1977; Ganapathy et al., 1985; Wilson et al., 1985). Reformulation of these equations for representation in the discrete spatial (z) and spatial frequency (k) domains will be illustrated using the transmembrane current per unit length as an example

$$I_m(P_q) = -\frac{1}{2\pi a\sigma_o} \sum_{n=0}^{N-1} i_m(Zn) e^{j2\pi nq/N} = -\frac{1}{2\pi a\sigma_o} DFT[i_m(Zn)] \tag{31}$$

$$i_m(Zn) = -2\pi a\sigma_o \frac{1}{N} \sum_{q=0}^{N-1} I_m(Pq) e^{-j2\pi nq/N} = -2\pi a\sigma_o\, IDFT[I_m(Pq)] \tag{32}$$

where

$$P = \frac{2\pi}{NZ}. \tag{33}$$

Here Z and P are the sampling intervals in the z- and k-domains, respectively, and n and q are integers. The function $i_m(z)$ is approximately band-limited in both the z- and k-domains, meaning that $i_m(z)$ is nonzero for a small finite range of z values ($-Z_1 < z < Z_2$) and essentially zero outside this range. Similarly, $i_m(z)$ is band-limited with respect to frequency content; therefore $I_m(k)$ is nonzero only within a small range $|k| < M$ (a constant) and essentially zero elsewhere. Thus, the discrete functions

$i_m(Zn)$ and $I_m(Pq)$ approach zero as Zn and Pq, respectively, become large. The sampling interval Z is chosen to be small enough so that no aliasing occurs in the k-domain, and the number of samples or sampling duration, NZ, is chosen to include the entire signal. Relationships similar in form to the DFT pair of equations (i.e., Eqs. 31 and 32) exist for $I_L^o(z)$ and $F_L^o(k)$ as well as $I_L^i(z)$ and $F_L^i(k)$.

Thus the various cable equations can be evaluated as products of DFTs (equivalent to linear convolution). Once again the transmembrane current is given as an example.

$$I_m(Pq) = F_m(Pq)C_{mo}(Pq, a, b), \tag{34}$$

where $q = 1 \ldots . N$. The transmembrane current itself is given by

$$i_m(Zn) = -2\pi a\sigma_o IDFT[I_m(Pq)]. \tag{35}$$

The other cable equations are also evaluated in a similar fashion using DFTs.

The equivalent filtering approach is illustrated in Fig. 1 for the case where extracellular potential is evaluated; the filters involved in the calculation are the membrane filter $M(|k|)$ and the medium filter $W_o(|k|\ \rho, b)$ for a cylindrical volume conductor of radius b. The input to the membrane filter is the spatial distribution of the transmembrane potential along the nerve fiber $\Phi_m(z)$. This is the potential distribution present across the equivalent cell membrane of the nerve fiber, along its entire length at an instant of time. The membrane filter transforms the spatial transmembrane potential distribution into the spatial potential distribution on the surface of the nerve fiber $\Phi_{so}(z)$, which in turn serves as input to the medium filter that produces the spatial potential distribution in the volume conductor medium at a particular radius ρ. Specifying a number of values of ρ, the potential distribution throughout the external volume conductor medium may be easily determined. The spatial current distributions $i_m(z)$ and $I_L^o(z)$ associated with the classical cable equations may be evaluated in a similar fashion at any instant of time provided the transmembrane potential distribution is specified at that instant of time.

The filters used in this technique are time-invariant and depend on certain electrical and geometrical parameters. Only the model input, namely the spatial transmembrane potential $\Phi_m(z)$ changes with time; and it may be different at different instants of time. This fact may be exploited when the extracellular currents and potentials are reconstructed as functions of time in that the filter functions need only be calculated once in the entire process for any given geometric and electrical configuration. Therefore, the particular spatial transmembrane potential distribution at each instant of time is presented as input to the field theoretic model and output is returned consisting of the desired current or potential distribution at that particular time instant.

Models for the Active Source Fiber

Our study involves an investigation of the nature of the potential and current density fields in a cylindrical volume conductor surrounding an active nerve fiber. In previous studies of Clark and Plonsey (1966, 1968), rather simple simulated action potential distributions were used as membrane source potential waveforms for the volume conductor problem. In the present study, spatial distributions of transmembrane potential $\Phi_m(z)$ are obtained from a distributed parameter model simulation of the active myelinated nerve fiber. These simulations yield much more realistic action potentials and the model parameters may be conveniently varied so as to represent a variety of experimental conditions. Fig. 2 *a* shows the equivalent circuit model for the representative myelinated nerve fiber.

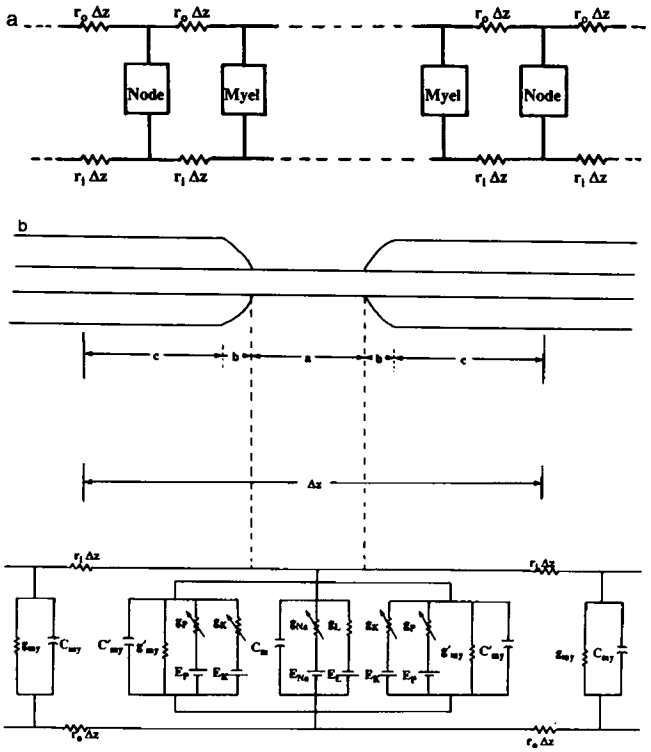

FIGURE 2 The (*a*) distributed parameter model and (*b*) the electrical network describing membrane patches of the myelinated nerve fiber. The patches of membrane in *a* are characterized by a modified Frankenhaeuser-Huxley model at the nodes and a parallel RC network in the internodal region. In *b* C_m is the specific membrane capacitance ($\mu F/cm^2$), E_L, E_{Na}, E_K, and E_P are the leak potential, sodium Nernst potential, potassium Nernst potential, and the Nernst potential of the nonspecific ion channel (mV), respectively, and g_L, g_{Na}, g_K, and g_P are the specific conductances (mS/cm^2) of the leak channel, the sodium channel, the potassium channel, and the nonspecific ion channel respectively, C'_{my} and g'_{my} are the specific capacitance and the specific conductance associated with the myelin sheath adjacent to the node, C_{my} and g_{my} are the specific myelin capacitance and conductance respectively, and r_i and r_o are the lumped resistance per unit length (Ω/cm) of the intra- and extracellular media, respectively. The myelinated fiber is shown on top where the regions are labeled as *a* for the nodal region, *b* for the paranodal region, and *c* for the internodal region.

The model is characterized by patches of membrane, coupled by resistances $r_i\Delta z$ and $r_o\Delta z$, where Δz represents a unit segment along the fiber; r_i and r_o are resistances per unit length. The shunt elements representing nodes of Ranvier are characterized by the Frankenhaeuser-Huxley model of the myelinated nerve (Frankenhaeuser and Huxley, 1964), with an additional shunt element to account for the myelin sheath adjoining the node of Ranvier on either side. The internodal region between two nodes of Ranvier is represented by a parallel RC circuit. The conductance and capacitance values used are those in accordance with the specific conductance and the specific capacitance of the myelin sheath. This representation of the myelinated nerve fiber is based on the work of Goldman and Albus (1968). The Frankenhaeuser-Huxley membrane model used by Goldman and Albus (1968) consists of three ionic currents and one leak current that are assumed to be present in the nodal membrane of the myelinated fiber. The three ionic currents consist of a fast inward sodium current, a delayed outward potassium current, and a very small inward current that is considerably slower than the fast sodium current. This later current is said to be due to nonspecific ions but is characterized in the model as a sodium current. Since experimental evidence (Horakova et al., 1968; Chiu et al., 1979; Brismar, 1980; Kocsis and Waxman, 1980) has proved the existence of potassium channels in the paranodal region and their almost complete absence in the node, we decided to associate the potassium and the nonspecific inward current in the membrane model with the paranodal region; the segments in the internodal region of the fiber are characterized by lumped parallel resistive capacitive elements as in Goldmann and Albus (1968). An equivalent circuit model of the nodal, paranodal, and internodal regions of the myelinated nerve fiber is shown in Fig. 2 *b*.

The parabolic partial differential equation describing the propagation of a nerve impulse along these distributed parameter networks is given as

$$\frac{\partial^2 V(z,t)}{\partial z^2} = 2\pi a(r_i + r_o)\left[C_m \frac{\partial V(z,t)}{\partial t} + i_{ion} - i_{stim}\right], \quad (36)$$

where V is the transmembrane voltage, C_m is the membrane capacitance, i_{ion} the total ionic current, and i_{stim} is the stimulus current density. The parabolic partial differential equation is numerically integrated by a stable, implicit technique known as the Crank-Nicholson method (Crank and Nicholson, 1947). The formulation must include boundary conditions at either ends of the fiber, and in this case the ends are considered to be sealed, reprsenting an infinite resistance to longitudinal current flow and hence,

$$\frac{\partial V}{\partial z}(0,t) = \frac{\partial V}{\partial z}(L,t) = 0, \quad (37)$$

where L is the length of the fiber.

The resulting set of $N + 1$ equations for a cable with N segments is reproduced in matrix form, thus

$$\begin{bmatrix} -2 & 4+\theta & 0 & 0 & 0 & 0 & 0 & 0 \\ 1 & \theta & 1 & 0 & 0 & 0 & 0 & 0 \\ 0 & 1 & \theta & 1 & 0 & 0 & 0 & 0 \\ \cdot & \cdot & \cdot & \cdot & \cdot & \cdot & \cdot & \cdot \\ \cdot & \cdot & \cdot & \cdot & \cdot & \cdot & \cdot & \cdot \\ \cdot & \cdot & \cdot & \cdot & \cdot & \cdot & \cdot & \cdot \\ 0 & 0 & 0 & 0 & 0 & 1 & \theta & 1 \\ 0 & 0 & 0 & 0 & 0 & 0 & 4+\theta & -2 \end{bmatrix} \cdot \begin{bmatrix} V_{0,j+1} \\ V_{1,j+1} \\ V_{2,j+1} \\ \cdot \\ \cdot \\ \cdot \\ V_{N-1,j+1} \\ V_{N,j+1} \end{bmatrix} = \begin{bmatrix} \phi_{1,j} \\ \phi_{1,j} \\ \phi_{2,j} \\ \cdot \\ \cdot \\ \cdot \\ \phi_{N-1,j} \\ \phi_{N-1,j} \end{bmatrix}, \quad (38)$$

where the terms θ and ϕ are specified in Table II. The tri-diagonal form of the matrix on the left-hand side of Eq. 38 may be easily inverted to solve for the vector $\underline{V}$, which is the transmembrane voltage at every point along the fiber, for each instant of time.

COMPUTATIONAL ASPECTS

To obtain the spatial transmembrane potential distribution along the fiber at each instant of time, the distributed parameter model characterizing the myelinated nerve fiber is evaluated. This simulation of the myelinated nerve fiber is run for a predetermined length of time for a given length of the nerve fiber, which implies that a certain fixed number of "time portraits" of the electrical activity along the fiber can be generated. Each one of these time portraits is a spatial transmembrane potential distribution. To reconstruct the extracellular currents and potentials, each of these time portraits is presented to the field theoretic model and the corresponding extracellular current or potential distribution is returned. Given an adequate (Nyquist) sampling rate in time, the resulting set of time portraits of the extracellular currents and potentials completely define the extracellular currents and potentials as functions of time.

The process of reconstruction of the time waveform is further simplified by the fact that there exists a basic set of spatial transmembrane potential distributions that repeat with time. The number of members in this set depends on the velocity of propagation of the electrical activity along the nerve fiber, the spatial sampling interval Δz, and the sampling interval in time Δt. Under normal conditions of conduction, this set consists of very few members that are needed to completely specify the extracellular potentials and currents at any given spatial point along the nerve, for

any instant of time. All the time portraits of the transmembrane potential that are generated by the distributed parameter model simulation of the myelinated nerve fiber are therefore not required as input to the field theory model. During abnormal conduction, however, the number of spatial transmembrane potential distributions required increases several-fold, depending upon the extent of the region of abnormality. A large region of abnormality results in the distortion of several representative spatial waveforms through the region and most of these need to be included in the basic set for a successful reconstruction.

Slowed conduction can be introduced by simulating paranodal demyelination which not only changes the myelin-specific capacitance and conductance on either side of the node, but also strengthens the potassium and nonspecific currents from the exposed area of the paranodal region. Complete conduction block may also be induced in this manner. The various values of the parameters used in the simulation are given in Table I, which lists the standard set for both electrical and geometric parameters. The radius of the volume conductor b is specified as a multiple of the fiber radius a. The partial differential equation that describes the propagation of the electrical activity along the nerve is numerically integrated using a modified Crank-Nicholson method (Ganapathy et al., 1987). Table II lists the various parameters that are required to solve the matrix Eq. 38 using this method.

RESULTS

With the parameter values specified in Table I, the distributed parameter network for the myelinated nerve fiber can be solved to obtain the transmembrane potential difference

TABLE I
ELECTRICAL AND GEOMETRIC MODEL PARAMETERS

Parameter	Value used
Fiber radius (a)	0.0005 cm
Myelin thickness (at)	0.0002 cm
Length of a node of Ranvier (NL)	0.0004 cm
Internodal distance (INL)	0.2 cm
Radius of the volume conductor (b)	$n \cdot a$
External resistivity (R_o)	70 Ω cm
Internal resistivity (R_i)	100 Ω cm
External resistance per unit length (r_o)	$R_o/\{\pi a^2(n^2 - 1)\}$
Internal resistance per unit length (r_i)	$R_i/\pi a^2$
Membrane capacitance (C_m)	$2\mu F/cm^2$
Myelin capacitance (C_{my})	$0.00387\ \mu F/cm^2$
Myelin conductance (g_{my})	$0.083308\ \mu S/cm^2$
Leak potential (E_l)	0.026 mV
Leak conductance (g_l)	$30.3\ mS/cm^2$
Sodium permeability constant (P_{Na})	0.008 cm/s
Potassium permeability constant (P_K)	0.0012 cm/s
Nonspecific permeability constant (P_P)	0.00054 cm/s
External sodium concentration ($[Na^+]_o$)	114.5 mM
Internal sodium concentration ($[Na^+]_i$)	13.74 mM
External potassium concentration ($[K^+]_o$)	2.5 mM
Internal potassium concentration ($[K^+]_i$)	120.0 mM

TABLE II
CRANK-NICHOLSON PARAMETER VALUES

Parameter	Defining expression or value
Step size in time (Δt)	0.005 ms
Step size in space (Δz)	0.02 cm
α for unmyelinated node	$[C_m K_1 NL + (\Delta z - NL)C_{my}K_2]/(\Delta z \Delta t)$
α' for the myelinated node	$K_2 C_{my}/\Delta t$
$W_{i,j}$	$(i_{Na} + i_K + i_p + i_l)(NL/\Delta z)$
$W^{my}_{i,j}$ for unmyelinated node	$V \cdot g_{my} \cdot (\Delta z - NL)/\Delta z$
$W'_{i,j}$ for myelinated node	$V \cdot g_{my}$
$\gamma_{i,j}$ for the unmyelinated node	$K_1 W_{i,j} + K_2 W^{my}_{i,j}$
$\gamma'_{i,j}$ for myelinated node	$K_2 W'_{i,j}$
θ for unmyelinated node	$-(2 + \alpha)$
θ' for myelinated node	$-(2 + \alpha')$
$\phi_{i,j}$ for unmyelinated node	$-V_{i-1,j} + (2 - \alpha)V_{i,j} - V_{i+1,j} + \gamma_{i,j}$
$\phi'_{i,j}$ for myelinated node	$-V_{i-1,j} + (2 - \alpha')V_{i,j} - V_{i+1,j} + \gamma'_{i,j}$

$K_1 = 4\pi a[r_i + (n^2 - 1)r_o](\Delta z)^2$; $K_2 = 4\pi(a + at)[r_i + (n^2 - 1)r_o](\Delta z)^2$.

at every point along the fiber for any time instant desired. The solution is shown as a three-dimensional view in Fig. 3 where the transmembrane potential is shown along a small length of the fiber, covering five nodes of Ranvier. The spatial transmembrane potential can be seen along the isochronal lines in the figure; electrical activity is shown here as propagating in the negative z-direction. The familiar action potential is seen in the transmembrane potential as a function of time, at a fixed point in space. The discontinuous nature of the propagation velocity along the nerve fiber manifests itself as discontinuities in the spatial waveform, which can be traced along each isochronal line.

The extracellular potential calculated at the fiber surface as a function of time, at different points along the nerve fiber, is shown in Fig. 4. The magnitude of the calculated potential at the nodes of Ranvier is 10 times its value at the internodes (note scale changes in Fig. 4). The discontinuous nature of the propagation is illustrated more

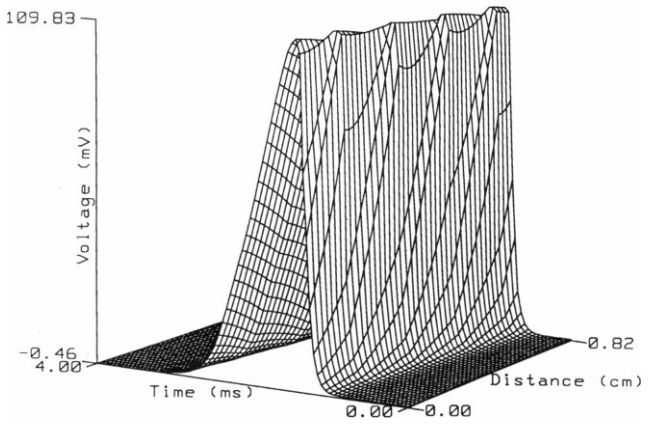

FIGURE 3 A three-dimensional view of the propagating action potential, propagating from right to left along the spatial axis (negative z-direction). The activity is shown over a time period of 4 ms and a spatial distance of 0.82 cm, which includes five nodes of Ranvier.

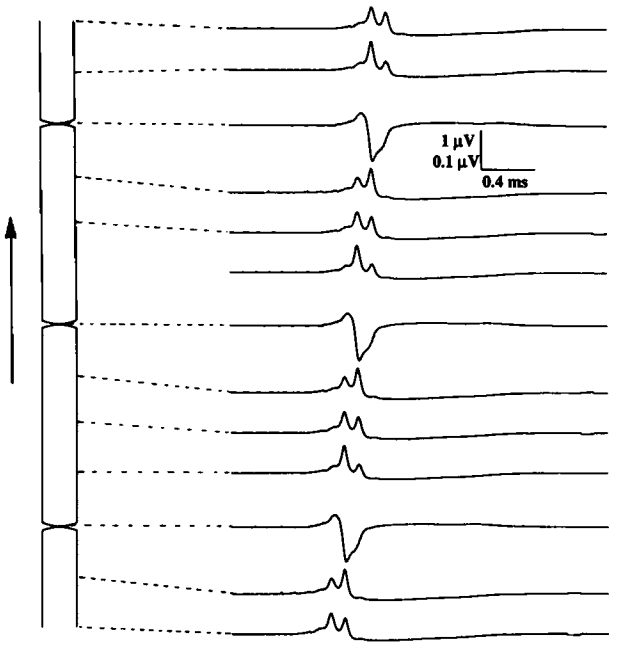

FIGURE 4 The values of extracellular potential as a function of time at several points on the surface of the nerve fiber. The potentials at the nodes of Ranvier are plotted on a scale 10 times the scale at which the potentials in the internodal region are drawn. The arrow indicates the direction of propagation of the electrical activity along the fiber.

clearly in this figure where the activity is proceeding from bottom to top along the fiber.

Fig. 5 is a three-dimensional view of the transmembrane current per unit length i_m. Upward currents in the figure are inward membrane currents, therefore the current spikes seen pushing out of the plane are inward currents. The troughs seen in the figure represent outward current. It can be seen that there is a strong inward current at the nodes of Ranvier followed by a prolonged outward current. At the internodal points along the fiber the current is completely outward and is 10 times smaller in magnitude than the peak to peak current at the nodes. Once again the propagation is in the negative z-direction, which means that the activity is traveling from right to left along the fiber.

A three-dimensional plot of the total longitudinal current outside the fiber (I_L^o) is presented in Fig. 6 where this current has been reversed in polarity for clarity of view. The total longitudinal current outside the fiber I_L^o is essentially a negatively directed current in both the nodal and the internodal regions. Propagation in Fig. 6 occurs in the same direction as that exhibited in Figs. 3 and 5 (i.e., in the negative z-direction) and therefore I_L^o being a negatively directed current, flows in the opposite direction. Observing Fig. 6 one will note that the strength of this current drops slightly at the nodes of Ranvier where the transmembrane current per unit length is strongest. The latter effect is best seen in Fig. 7.

Fig. 7 *a* shows the transmembrane current per unit length as a function of time, at several points along the fiber. These spatial points correspond to those that were considered when the extracellular potential on the outer surface of the fiber was shown in Fig. 4. The current waveforms at the nodes are plotted on a scale 10 times the magnitude of the scale used to plot the currents at the internodes. As can be easily seen on comparing Figs. 4 and 7 *a*, the extracellular potential on the outer surface of the fiber follows the transmembrane current per unit length very closely, which is not surprising when it is recalled that the extracellular medium is treated in this model as a simple resistive medium.

The total longitudinal current outside the fiber is shown as a function of time at the same spatial points as those used in Figs. 4 and 7, *a* and *b*. As stated before, it can be seen here that the longitudinal current decreases in magni-

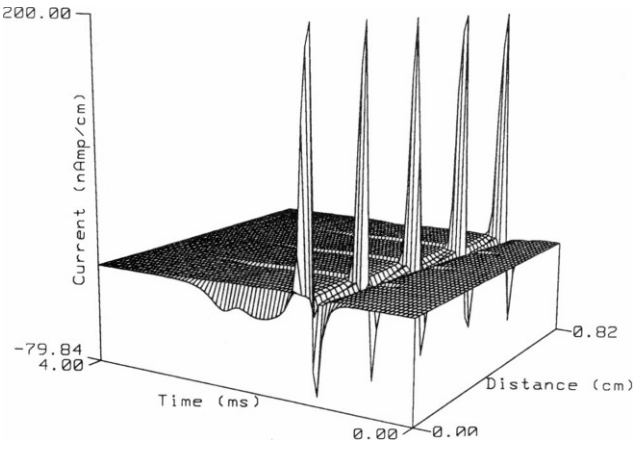

FIGURE 5 A three-dimensional view of the transmembrane current per unit length across the equivalent cell membrane of the fiber. The polarity of the current has been reversed so that troughs represent outward currents and spikes inward currents. Propagation is from right to left along the spatial axis and the activity is shown for a time period of 4 ms over five nodes of Ranvier.

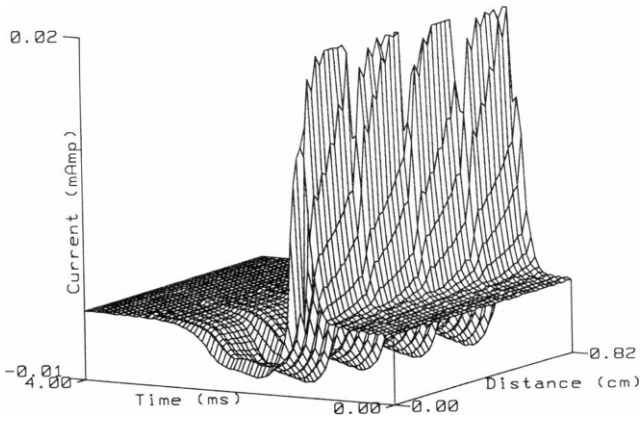

FIGURE 6 A three-dimensional view of the total longitudinal current outside the nerve fiber. The polarity of the current is such that troughs represent positive currents and spikes negative currents. Propagation is from right to left along the spatial axis (negative z-direction).

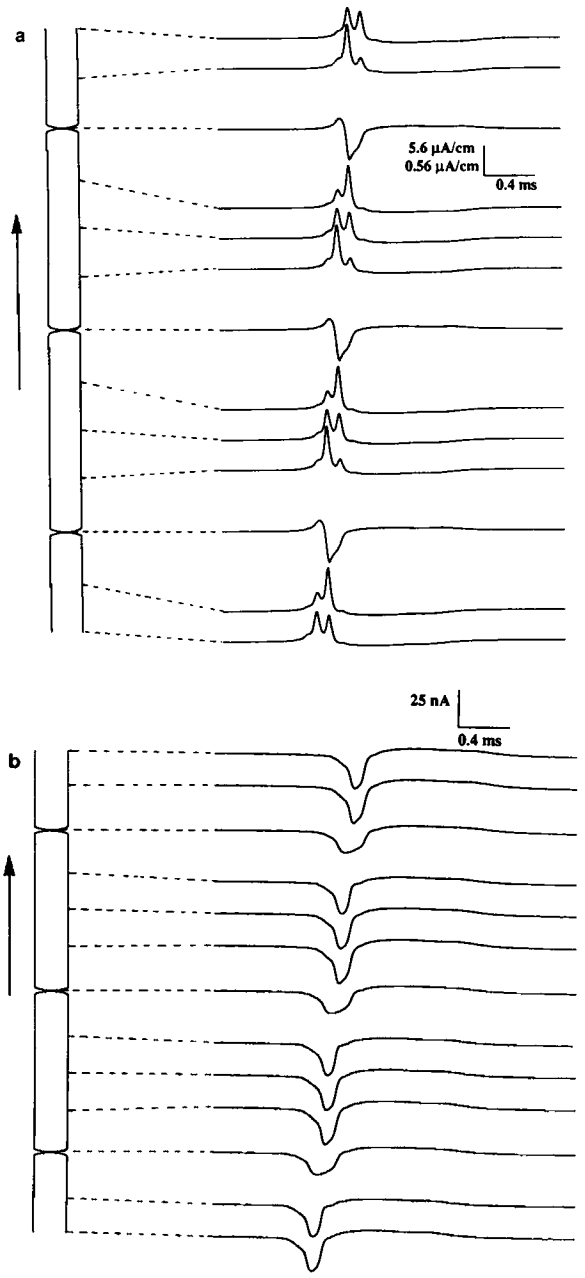

FIGURE 7 The calculated current waveforms for (*a*) the transmembrane current per unit length and (*b*) the total longitudinal current outside the fiber as functions of time at several points on the surface of the fiber. In *a* the current values at the nodes are on a scale 10 times that used for the waveforms at the internodal points. The propagation of electrical activity is from bottom to top along the fiber as indicated by the arrows.

tude at the nodes; however, the difference in magnitude is not as significant as in the case of the transmembrane current or the extracellular potential. For example, the total longitudinal current in the internodal region is only twice as much as its value at the nodes. The discontinuous nature of the propagation of the electrical activity along the myelinated fiber is very prominent in Fig. 7 where the electrical activity is shown moving from bottom to top along the fiber.

When experimental measurements of current are made, the procedure is to record the voltage at two points along the myelinated fiber and from this differential voltage measurement, first the total longitudinal current and then the transmembrane current per unit length are estimated (Paintal, 1965, 1966; Rasminsky and Sears 1972; Bostock and Sears, 1978). To study the effects of this technique on the current finally evaluated, we simulated the same approximation scheme in our model. Fig. 8 is an illustration of the total longitudinal current obtained by using the extracellular potential difference between two points that were 120 μm apart, and dividing the difference by the resistance per unit length of the volume conductor medium (r_o). This approximates the well-known cable equation formula $I_L^o(z) = -1/r_o[\partial V^o(z)/\partial z)]$. By taking the difference of two values of the longitudinal current obtained at points 120 μm apart and dividing the result by the distance between the two points, an estimate of the transmembrane current per unit length is found. On the left-hand side of Fig. 8 several longitudinal current waveforms are plotted in this fashion. To the right of these waveforms is an estimate of the transmembrane current per unit length found using the same differencing technique on the longitudinal current waveforms at the left. The results obtained in this fashion agree very well with the results predicted by our model. All the calculations seen in Fig. 8 were performed for a volume conductor radius $b = 30a$.

When the external volume conductor is reduced in extent, i.e., when the value of b is made to approach that of the fiber radius a, the calculated extracellular potential waveforms are considerably larger in peak to peak magnitude. The same differencing scheme that was used in obtaining the results in Fig. 8 may be repeated for different values of the volume conductor radius as well as for

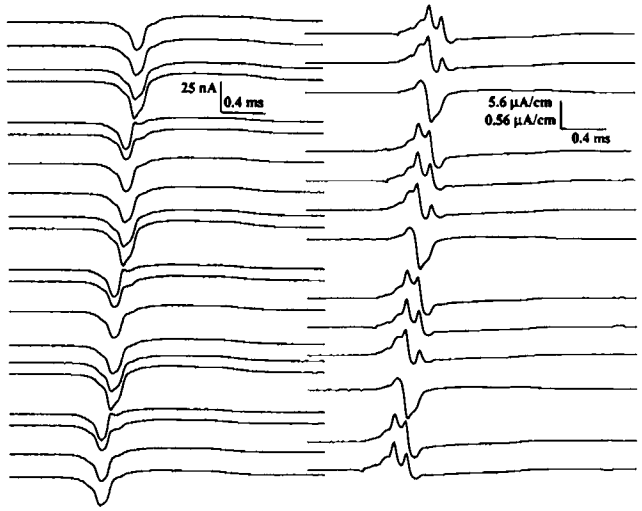

FIGURE 8 Estimates of total longitudinal current and transmembrane current per unit length as functions of time at several points along the fiber. These estimates were made with an electrode separation of 120 μm. See text for details.

different values of separation distance between the values used to estimate the current waveforms. Changing the separation distance between the values used to estimate the currents is equivalent to changing the separation distance of the electrodes used to make the differential recording experimentally. The results of this simulation are shown in Fig. 9 *A* for the longitudinal current and Fig. 9 *B* for the transmembrane current per unit length. In both *A* and *B* of Fig. 9 the first column corresponds to an electrode separation of 200 μm, the center column to a separation distance of 400 μm, and the third column to a separation distance of 600 μm. In all cases we found that the estimate made with an electrode separation of 200 μm agreed very well with the calculated value at that point, both for the total longitudinal current and the transmembrane current per unit length. When the volume conductor radius was reduced both the total longitudinal current and the transmembrane current per unit length increased in magnitude. The estimates made for the current waveforms using an electrode separation larger than 200 μm resulted in an under-determination of the current magnitude. The extent by which the total longitudinal current was underestimated reduced when the volume conductor boundary approached the fiber surface. This effect was apparent to a much smaller extent in the case where the transmembrane current per unit length was estimated. All these estimates were made with the electrodes centered about the node.

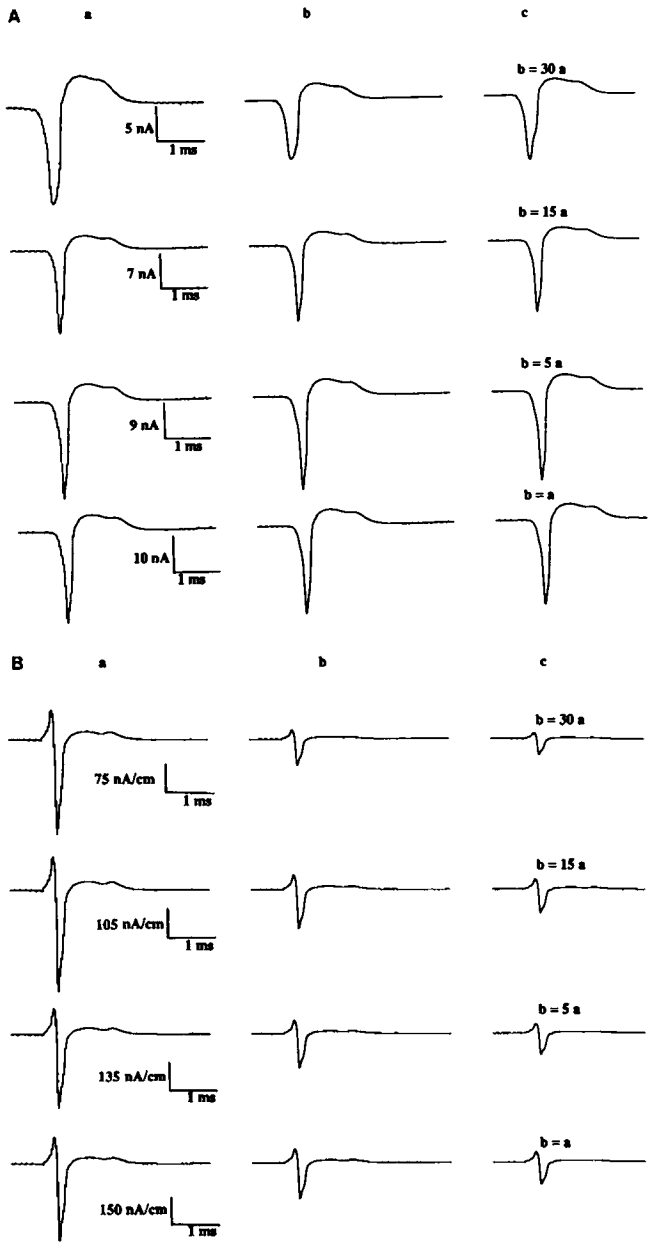

FIGURE 9 Estimates of (*A*) total longitudinal current outside the fiber and (*B*) the transmembrane current per unit length as functions of time for different electrode separations and various volume conductor extents. In both cases, column *a* corresponds to an electrode separation of 200 μm, column *b* to an electrode separation of 400 μm, and column *c* to an electrode separation of 600 μm. The various rows correspond to the different values of volume conductor radius *b*.

When the node was not centered between the electrodes the estimate was found to be underdetermined even when the electrode separation was 200 μm. Fig. 10 shows the results of a simulation where the pair of measurement electrodes was swept across the node of Ranvier from left to right, starting with the node centered between the pair of measurement electrodes up to a point when the left-hand side electrode is on the node. The estimated current waveforms are smaller in duration and amplitude when the node is no longer centered between the electrodes. As the positon of the node moves closer to the electrode on the left the waveform also shifts toward the left leading to an error in the estimated time of occurrence of the waveform. All three errors, namely the amplitude error, the duration error, and the time of occurrence error decrease with a reduction in the volume conductor extent. In the case of the estimated transmembrane current per unit length waveform, when the volume conductor extent is made zero, corresponding to the case where a thin adhering layer of conducting fluid is present around the fiber, the estimated current waveform is error-free even when the node is off-center by as much as 50 μm. The estimated longitudinal current is more sensitive to electrode positioning and under the same conditions it can be estimated correctly only when the node is off-center by <25 μm. The estimated transmembrane current per unit length can be correctly found for a volume conductor of radius $b = 30a$ even when the node is off-center by 25 μm, which is certainly not the case for the estimated total longitudinal current, as is clearly seen from Fig. 10 *a*. Under all circumstances we found that the estimated transmembrane current per unit length was less sensitive to electrode positioning than the estimated total longitudinal current waveform.

The effects of slowed conduction, simulated by inducing paranodal demyelination at one node in the cable, are shown in Fig. 11 *a* for the transmembrane potential distribution and in Fig. 11 *b* for the calculated transmembrane current per unit length; once again the spikes represent

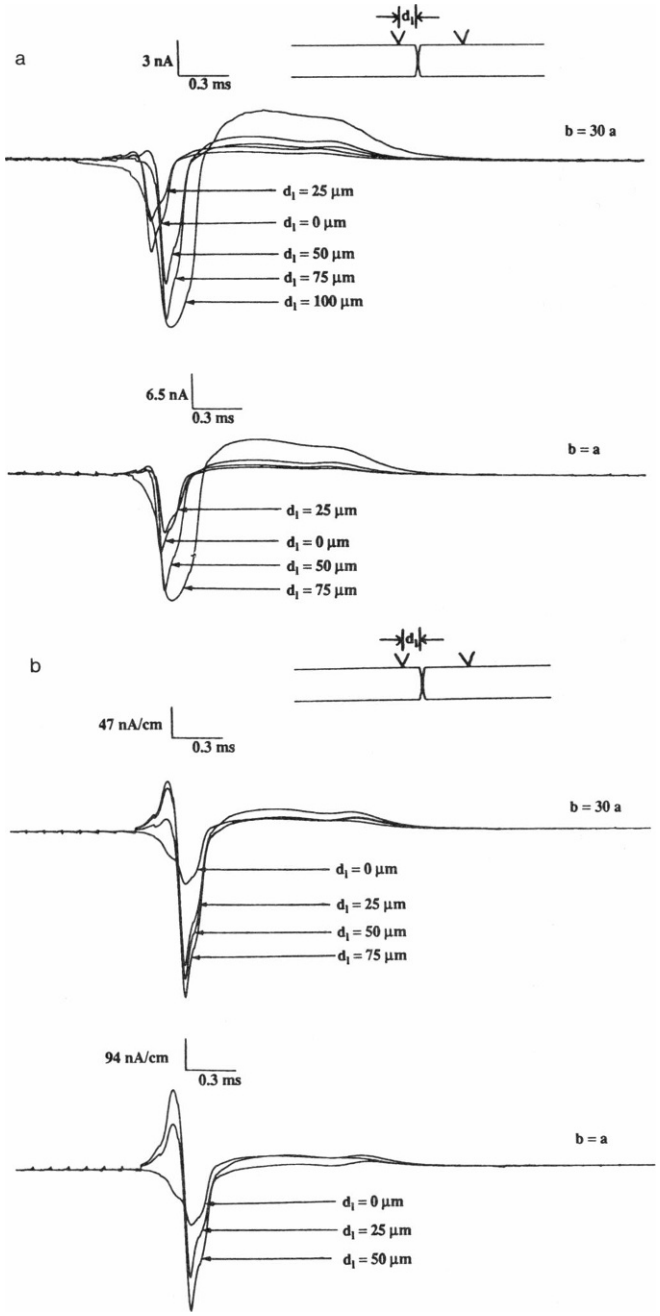

FIGURE 10 Estimates of (*a*) total longitudinal current outside the fiber and (*b*) the transmembrane current per unit length as functions of time; for two volume conductor extents when the pair of measurement electrodes is moved from left to right across a node of Ranvier. The distance d_1 is the separation distance between the node and the electrode on the left of the electrode pair as shown in the inset. The electrode separation is 200 μm.

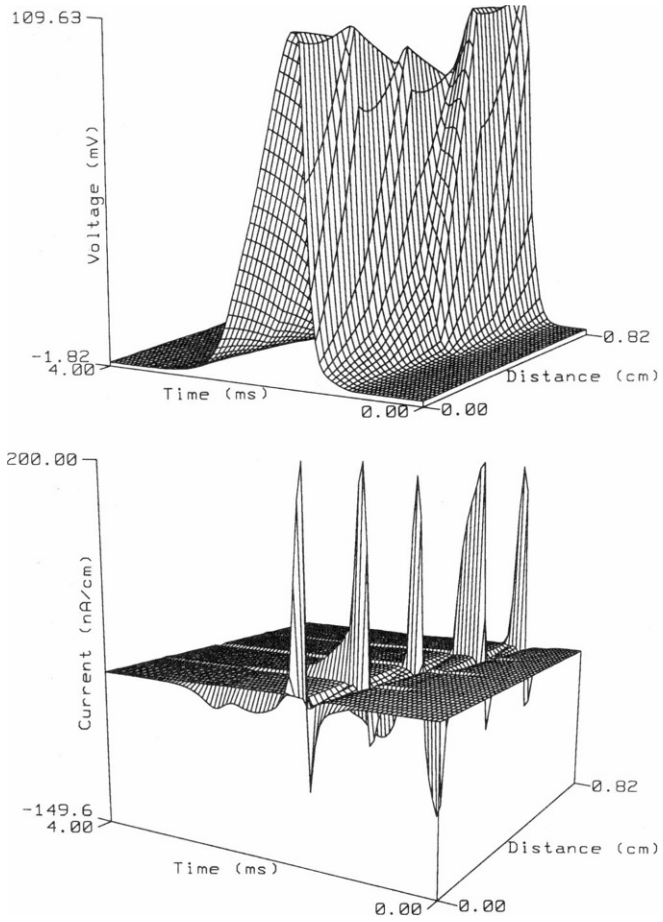

FIGURE 11 A three-dimensional view of (*a*) transmembrane potential and (*b*) calculated transmembrane current per unit length for slowed conduction induced by simulating paranodal demyelination at one node. The electrical activity is shown as propagating from right to left along the spatial axis. The current polarity is such that the upward spikes are inward membrane currents and the troughs are outward membrane currents.

inward current, troughs represent outward current, and conduction is in the negative *z*-direction. The results shown were obtained upon increasing the length of the paranodal region at the node by 10%. As expected, the transmembrane potential drops in magnitude as it reaches the abnormal region. The transmembrane current at the abnormal node has a very strong component of outward current as can be seen from the fairly well pronounced trough at that point (Fig. 11 *b*). We also found a prolongation of the inward current just before and just after the abnormal region. This is not a surprising result if it is recalled that one of the effects of slowed conduction is the prolongation of the action potential through the abnormal region. One of the consequences of the broadening of the action potential is to prolong the voltage drive on the sodium channel, thereby prolonging the inward current. Also as the electrical activity crosses the abnormal region, there is an abrupt slope change in the spatial waveform through that region as a consequence of the change in conduction velocity. The resulting strong discontinuity in the transmembrane potential waveform is emphasized in the transmembrane current record.

The effects of slowed conduction on the transmembrane current per unit length and the total longitudinal current outside the fiber are seen very distinctly in Fig. 12, *a* and *b*. The electrical activity is shown as propagating from bot-

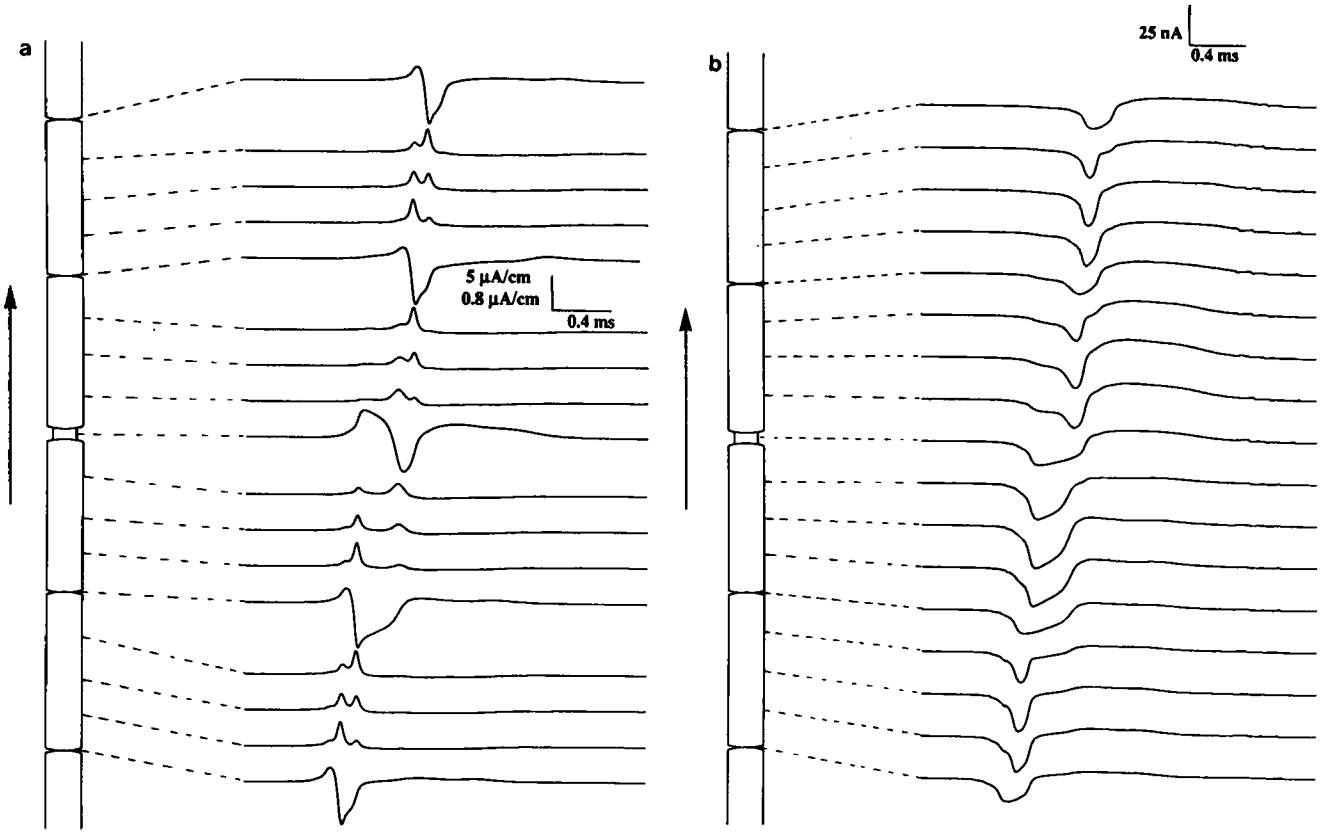

FIGURE 12 The calculated current waveforms for (*a*) the transmembrane current per unit length and (*b*) the total longitudinal current outside the fiber as functions of time at several points on the surface of the fiber for the case of slowed conduction. In *a* the current values at the nodes are on a scale about six times that used for the waveforms at the internodal points. The propagation of electrical activity is from bottom to top along the fiber as indicated by the arrows.

tom to the top of the fiber. Fig. 12 shows that both the transmembrane current per unit length and the total longitudinal current waveforms are distorted as the activity propagates into the abnormal region. The decrease in the velocity of propagation is very prominent in both figures, and both waveforms are smeared in time as they pass through the abnormal region. The waveform shapes are restored to normal by the time the activity reaches the node that is distant one node beyond the abnormal node. The records shown in Fig. 12 are in general agreement with the experimental findings of Bostock and Sears (1978). The extracellular potential waveforms faithfully follow the transmembrane current per unit length waveforms, which is as it should be for a passive, resistive external medium.

Fig. 13 shows the calculated extracellular field potential as a function of time at a point directly above a node of Ranvier for normal conduction in *a* and for slowed conduction in *b*. With increasing distance from the fiber surface the extracellular potential falls in magnitude and frequency content for both normal and abnormal conduction. In the case of abnormal conduction the calculated extracellular potential has a strong positive peak reflecting the presence of the strong outward current. The extracellular potential also has a second positive peak that corresponds

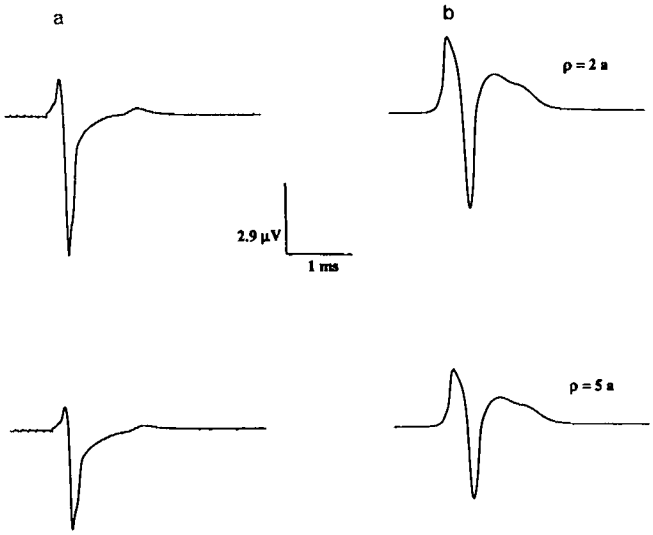

FIGURE 13 The extracellular potential as a function of time at a distance equal to the fiber radius and four times the fiber radius from the fiber surface, directly above a node of Ranvier. The node considered is the central node in the simulation when the propagation of electrical activity is (*a*) normal and (*b*) slowed. In the case of slowed conduction, the node considered here is the single node at which paranodal demyelination has been induced.

to the hyperpolarization seen in the transmembrane potential at the end of the action potential.

DISCUSSION OF RESULTS

In this paper we have shown that it is possible to reconstruct the extracellular currents and potentials as functions of time using a simple and efficient filter theory approach. The resulting currents and potential waveform correspond well with experimental values in literature. Also simulated is the experimental technique that is used to measure currents in practice. The results of the simulation indicate that electrode separation and placement are critical factors when such measurements are made. The node of Ranvier must be centered between the electrodes for the estimate of current magnitudes to be correct. Decreasing the extent of volume conductor (Fig. 9) makes electrode separation a less critical factor for the estimation of the total longitudinal current, but this improvement is not as apparent for the case of the transmembrane current per unit length.

Electrode positioning (Fig. 10) was found to be a critical factor for obtaining error-free estimates when relatively large volume conductors were considered. With a decreasing volume conductor extent, the position of the node relative to the two measuring electrodes was found to be less critical. This can be explained upon noting that with a decreasing volume conductor extent the extracellular potentials tend to be larger in magnitude and spatial duration. Fig. 14 shows the characteristics of the membrane and medium filter functions when the volume conductor radius is varied. The membrane acts as a second derivative filter and so the shape of the membrane filter characteristic is a family of parabolas as seen from Fig. 14 *a*. As the outer boundary of the volume conductor is decreased, the membrane filter characteristic no longer approaches zero as the spatial frequency k tends to zero, as in the infinite medium case. Rather as b becomes smaller the membrane filter gain at low spatial frequencies increases (Fig. 14 *a*, *inset*). The medium filter characteristic shown in Fig. 14 *b* is computed at a field radius $\rho = 7a$ and has the nature of a low pass filter whose cut-off frequency decreases as the volume conductor radius is increased. Thus, the filter characteristics of both filters show an increase in lower spatial frequency gain as the outer boundary of the volume conductor is made smaller. This increase in lower spatial frequency gain results in a larger signal magnitude and a larger spatial extent of the signal (a larger spatial extent corresponds to an increase in the lower spatial frequency content of the signal). The difference between the potentials at two closely spaced points along the fiber is therefore less significant under these circumstances, making the effects of slight shifts in electrode positioning negligible.

The effects of slowed conduction are seen in the transmembrane potential, the transmembrane current, and the calculated extracellular potential waveforms (Figs. 11–13). The method by which paranodal demyelination was

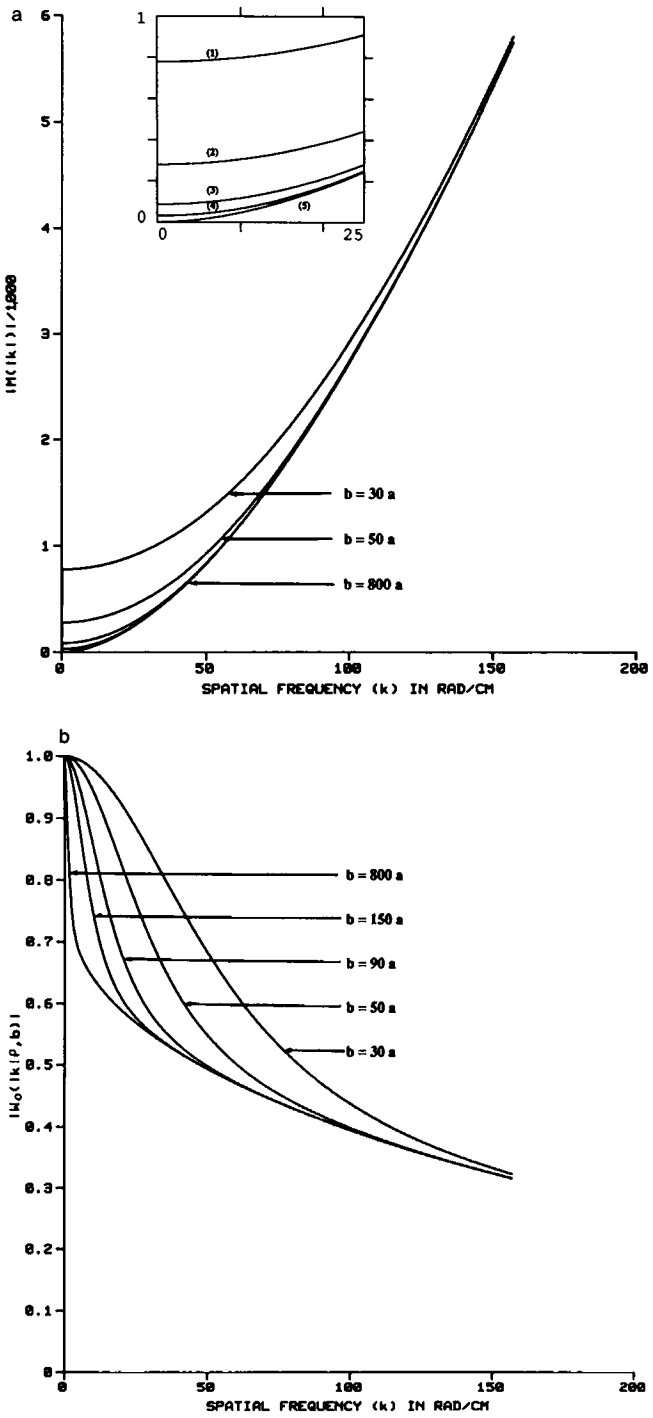

FIGURE 14 The characteristics of (*a*) the membrane filter function $M(|k|)$ and (*b*) the medium filter function $W_0(|k|\,\rho, b)$ vs. k for various values of the volume conductor radius b. The case chosen is for a cylindrial myelinated fiber having a radius of 5 μm. In Fig. 14 *a* the characteristics are labeled in the inset as (*1*) for $b = 30a$, (*2*) for $b = 50a$, (*3*) for $b = 90a$, (*4*) for $b = 150a$, and (*5*) for $b = 800a$. The medium filter is evaluated at a field radius $\rho = 7a$.

simulated results in the strengthening of the outward potassium currents from the paranodal regions of the abnormal node. This is reflected in the prolonged trough seen in the transmembrane current per unit length waveform of Figs. 11 *b* and 12 *a* and also in the strong second positive peak of the extracellular potential waveform of Fig. 13, column *b*. The calculated extracellular potential waveforms are in general of the same shape as the transmembrane current per unit length, which is as it should be for a passive, resistive extracellular medium, and hence both reflect the prolonged outward current that exists at the abnormal node. The upstroke velocity of the action potential in the abnormal region decreases and this is reflected in the extracellular potential and the transmembrane current per unit length waveforms as a broadening of the first positive and negative peaks.

As stated before, the calculation technique described in this paper is quite rapid, involving a small fraction of the computational time required by a comparable finite difference or finite element characterization of the myelinated nerve fiber's immediate surroundings. The field theory model can be easily modified to include one or more regions around the nerve fiber, each with varying degrees of anisotropy. This technique, which combines a distributed parameter model of the nerve fiber with a field theory model of its environment, can therefore be extended to the quantitative study of a number of intriguing problems in nerve electrophysiology including (*a*) the electric field stimulation of myelinated nerve and the subsequent determination of excitability thresholds, and (*b*) a more detailed study of nerve conduction in demyelination disease.

This work was supported by National Science Foundation grants BNS-8014052 and ECS-8405435.

Received for publication 19 May 1987 and in final form 31 July 1987.

REFERENCES

Abramowitz, M., and I. A. Stegun. 1965. Handbook of Mathematical Functions. Dover Publications, Inc., New York.

Barach, J. P., B. J. Roth, and J. P. Wikswo, Jr. 1985. Magnetic measurements of action currents in a single nerve axon: a core conductor model. *IEEE (Inst. Electr. Electron. Eng.) Trans. Biomed. Eng.* 32:136–140.

Bostock, H., T. A. Sears, and R. M. Sherratt. 1983. The spatial distribution of excitability and membrane current in normal and demyelinated mammalian nerve fibers. *J. Physiol. (Lond.).* 341:41–58.

Bostock, H., and T. A. Sears. 1978. The internodal axon membrane: electrical excitability and continuous conduction in segmental demyelination. *J. Physiol. (Lond.).* 280:273–301.

Brismar, T. 1980. Potential clamp analysis of membrane currents in rat myelinated nerve fibers. *J. Physiol. (Lond.).* 313:301–315.

Chiu, S. Y., J. M. Ritchie, R. B. Rogart, and D. Stagg. 1979. A quantitative description of membrane currents in rabbit myelinated nerve. *J. Physiol. (Lond.).* 292:149–166.

Clark, J. W., and R. Plonsey. 1966. A mathematical evaluation of the core conductor model. *Biophys. J.* 6:95–112.

Clark, J. W., and R. Plonsey. 1968. The extracellular potential field of the single active nerve fiber in a volume conductor. *Biophys. J.* 8:842–864.

Crank, J., and P. Nicholson. 1947. A practical method for the numerical evaluation of solutions of partial differential equations of the heat conduction type. *Proc. Camb. Philos. Soc. (Math. Phys. Sci.)* 43:50–67.

Frankenhaeuser, B., and A. F. Huxley. 1964. The action potential in the myelinated nerve fiber of Xenopus laevis as computed on the basis of voltage clamp data. *J. Physiol. (Lond.).* 171:302–315.

Ganapathy, N., J. W. Clark, O. B. Wilson, and W. Giles. 1985. Forward and inverse potential field solutions for cardiac strands of cylindrical geometry. *IEEE (Inst. Electr. Electron. Eng.) Trans. Biomed. Eng.* 32:566–577.

Ganapathy, N., J. W. Clark, and O. B. Wilson. 1987. Extracellular potentials from skeletal muscle. *Math. Biosci.* 83:61–96.

Goldman, L., and J. S. Albus. 1968. Computation of impulse conduction in myelinated fibers: theoretical basis of the velocity-diameter relation. *Biophys. J.* 8:596–607.

Greco, E. C., J. W. Clark, and T. L. Harman. 1977. Solution of the forward and inverse problems associated with the potential field of a single active nerve fiber in a volume conductor. *Math. Biosci.* 33:235–256.

Horakova, M., W. Nonner, and R. Stampfli. 1968. Action potentials and voltage-clamp currents of single rat Ranvier nodes. *Proc. Int. Union Physiol. Sci.* 7:198.

Kocsis, J. D., and S. G. Waxman. 1980. Absence of potassium conductance in central myelinated axons. *Nature (Lond.).* 287:348–349.

Paintal, A. S. 1965. Effects of temperature on conduction in single vagal and sapheneous myelinated nerve fibers of the cat. *J. Physiol. (Lond.).* 180:20–49.

Paintal, A. S. 1966. The influence of diameter of medullated nerve fibers of cats on the rising and falling phases of the spike and its recovery. *J. Physiol. (Lond.).* 184:791–811.

Rasminsky, M., and T. A. Sears. 1972. Internodal conduction in undissected demyelinated nerve fibers. *J. Physiol. (Lond.).* 227:323–350.

Roth, B. J., and J. P. Wikswo. 1985. The magnetic field of a single axon. A comparison of theory and experiment. *Biophys. J.* 48:93–109.

Wikswo, J. P., Jr., J. P. Barach, and J. A. Freeman. 1980. Magnetic field of a nerve impulse: first measurements. *Science (Wash. DC).* 208:53–55.

Wilson, O. B., J. W. Clark, Jr., N. Ganapathy, and T. L. Harman. 1985. Potential field from an active nerve in an inhomogeneous, anisotropic volume conductor. *IEEE (Inst. Electr. Electron. Eng.) Trans. Biomed. Eng.* 32:1032–1041.